Journal of Materials Chemistry A

ROYAL SOCIETY OF CHEMISTRY

PAPER

View Article Online
View Journal | View Issue

Cite this: J. Mater. Chem. A, 2023, 11, 12315

Solution-processed In_2Se_3 nanosheets for ultrasensitive and highly selective NO_2 gas sensors†

Gianluca D'Olimpio, ‡[a] Vardan Galstyan, ‡[bc] Corneliu Ghica,[d] Mykhailo Vorokhta,[e] Marian Cosmin Istrate,[d] Chia-Nung Kuo,[fg] Chin Shan Lue,[fg] Danil W. Boukhvalov, *[hi] Elisabetta Comini *[b] and Antonio Politano *[a]

In this work, we demonstrate that solution-processed In_2Se_3 nanosheets exhibit exceptional selectivity and sensitivity to NO_2 gas, making them a promising candidate for gas detection systems. Theoretical simulations and surface-science experiments reveal the unique surface properties of In_2Se_3 nanosheets, which prevent physisorption of oxygen, carbon monoxide, and carbon dioxide, making them remarkably stable towards oxidation and CO-poisoning. Moreover, we show that NO_2 molecules adsorb stably on In_2Se_3 nanosheets, particularly on Se vacancies, even at high temperatures. The coadsorption of water further enhances NO_2 sticking on the In_2Se_3 surface, making it an ideal material for gas sensing applications in humid and harsh environments. The fabricated In_2Se_3 gas sensors exhibit excellent and reversible sensing response to NO_2 gas, with a limit of detection of 5 ppb at 300 °C, and a highly selective response to NO_2 compared to other gases and volatile organic compounds. Our sensors outperform other two-dimensional (2D) semiconductors, metal oxides, and their heterostructures, thanks to the unique surface properties of In_2Se_3 nanosheets. Importantly, the number of layers and termination of the surface almost have no impact on the sensing performance of In_2Se_3, which is advantageous for practical applications. The high sensitivity, selectivity, and stability of In_2Se_3 nanosheets make them an exciting platform for the fabrication of high-performance gas sensors, particularly in harsh environments, such as industrial settings or outdoor monitoring. Moreover, our solution processing approach enables scalable production of the sensors. Additionally, their unique surface properties make them an attractive candidate for developing complex composite nanostructures with tailored gas sensing characteristics for various applications.

Received 6th March 2023
Accepted 11th May 2023

DOI: 10.1039/d3ta01390a

rsc.li/materials-a

1 Introduction

Air quality monitoring has become increasingly important, due to industrialization and global warming issues.[1–5] Various approaches have been developed for detecting toxic and hazardous gaseous compounds in the air, including chemoresistive gas sensors based on metal-oxide semiconductors.[6–10] These sensors are popular, due to their small size and easy operation mechanism, whereby changes in electrical parameters of metal oxides are used as a sensing signal, based on the adsorption of gas molecules on their surface.[6–8,11–18] However, to ensure high sensitivity, the sticking coefficient for the adsorption of gases on their surface should be maximized, while keeping the absolute value of the adsorption energy not too high to ensure adsorption/desorption of analytes. Moreover, the presence of different gaseous and volatile organic compounds in the air can cause variations in the conductance (or resistance) of metal oxides, affecting their selectivity to a specific analyte. These challenges continue to impact the sensitivity and selectivity of conventional chemical gas sensors, highlighting the need for novel functional materials to meet modern requirements.

Recently, 2D semiconductors have drawn attention for their large surface area, unique charge transport, and surface physicochemical properties, which make them promising candidates for gas sensing.[19–22] However, their performance in gas sensing

[a]Department of Physical and Chemical Sciences, University of L'Aquila, via Vetoio, 67100 L'Aquila, AQ, Italy. E-mail: antonio.politano@univaq.it
[b]Sensor Lab, Department of Information Engineering, University of Brescia, Via Valotti 9, 25133 Brescia, Italy. E-mail: elisabetta.comini@unibs.it
[c]Department of Engineering "Enzo Ferrari", University of Modena and Reggio Emilia, Via Vivarelli 10, 41125 Modena, Italy
[d]National Institute of Materials Physics, Atomistilor 405A, 077125 Magurele, Romania
[e]Charles University, V Holesovickäch 2, Prague 8, 18000 Prague, Czech Republic
[f]Department of Physics, National Cheng Kung University, 1 Ta-Hsueh Road, 70101 Tainan, Taiwan
[g]Taiwan Consortium of Emergent Crystalline Materials, National Science and Technology Council, Taipei 10601, Taiwan
[h]College of Science, Institute of Materials Physics and Chemistry, Nanjing Forestry University, Nanjing 210037, P. R. China. E-mail: danil@njfu.edu.cn
[i]Institute of Physics and Technology, Ural Federal University, Mira 19 Str., Yekaterinburg 620002, Russia

† Electronic supplementary information (ESI) available. See DOI: https://doi.org/10.1039/d3ta01390a

‡ These authors contributed equally.

is not yet comparable to that of metal oxides in terms of sensitivity, selectivity, response/recovery time, and long-term stability. Despite this, the wide range of 2D semiconductors[23,24] has not fully explored for gas sensing.

Among the various 2D semiconductors, In_2Se_3 is particularly noteworthy. It is III–VI semiconductor with a direct bandgap[25] and weak van der Waals interlayer bonds. In the past, In_2Se_3 has been studied for its capabilities as a broadband light absorber[26] and phase-change[27,28] material, with potential applications in broadband photodetection,[25,29–31] solar cells,[32] non-volatile memories,[33,34] and ferroelectric devices.[35–37] At room temperature, In_2Se_3 exists in five stable phases: α, β, γ, δ, and κ,[27,31,38–44] with α-In_2Se_3 having also two differently stacked polymorphs (2H and 3R[44,45]). Phase transitions between different structures can be induced through pressure and heating, making it a significant material for phase-change memories.[27,42,44] However, the layered 2D structure only appears in the α and β phases.[29]

Here, we report on the fabrication of novel gas sensors based on solution-processed In_2Se_3 nanosheets, showing superb selectivity and sensitivity for the detection of NO_2. The fabricated In_2Se_3 gas sensors exhibit excellent and reversible sensing response to NO_2 gas, with a limit of detection of 5 ppb at 300 °C, and a highly selective response to NO_2 compared to other gases and volatile organic compounds. Theoretical simulations and experiments reveal the unique surface properties of In_2Se_3 nanosheets, which prevent physisorption of oxygen, carbon monoxide, and carbon dioxide, making them remarkably stable towards oxidation and CO-poisoning. These findings make In_2Se_3 nanosheets an exciting platform for the fabrication of high-performance gas sensors in harsh environments.

2 Results and discussion

2.1 Atomic structure

The atomic structure of α-In_2Se_3 consists of non-covalently bonded In_2Se_3 units (Fig. 1a), each composed of two covalently bonded $InSe_2$ and InSe sub-units. The $InSe_2$ sub-unit displays an atomic structure similar to the 1T-structural phase of other diselenides, such as $MoSe_2$ (ref. 46 and 47) and VSe_2,[48,49] while the InSe sub-unit has an atomic structure, that can be described as an $InSe_2$ sub-layer missing Se atoms from one side. The In-terminated side of the InSe sub-layer is covalently bonded with Se atoms of the $InSe_2$ sub-layer, resulting in two different terminations corresponding to $InSe_2$ or InSe sub-layers on the surface. The surface termination type can only be recognized by side view (Fig. 1a), while, in the case of the monolayer, both sides are available for adsorption.

Single crystals of In_2Se_3 were grown by chemical vapour transport (see Methods) and their phase was determined by Raman spectroscopy (Fig. 1b) and X-ray diffraction (XRD, Fig. 1e) to be α-2H, belonging to the $P6_3mc$ space group, which differs from the α-3R phase ($R3m$ space group). The spectroscopic fingerprint of the α-2H phase is the E^2 phonon at

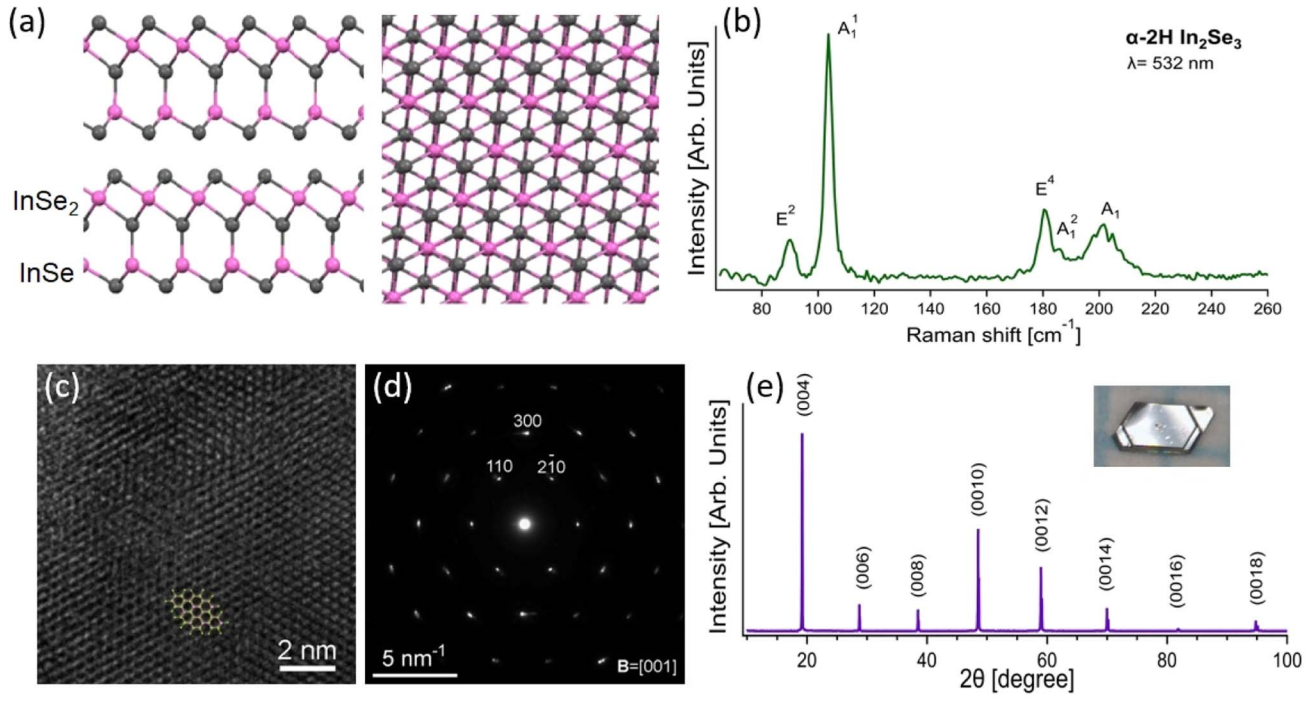

Fig. 1 Structural and spectroscopic characterization of α-2H In_2Se_3. (a) Side and top view of a single crystal of α-2H In_2Se_3, where grey and pink balls represent Se and In atoms, respectively. (b) Raman spectrum of α-2H In_2Se_3 acquired with $\lambda = 532$ nm, with the corresponding assignment of each Raman-active mode. Prior studies were consulted for the mode assignments.[37,44,50] (c) High-resolution transmission electron microscopy (HRTEM) image, showing atomic-level details of the crystal structure (taken at the bottom-right side of the box in Fig. 3b), with an overlaid atomic model of the α-2H In_2Se_3 crystal in a [001] projection. (d) Selected area electron diffraction (SAED) pattern, demonstrating the single-crystalline nature of the sample. (e) X-ray diffraction (XRD) pattern of an α-2H In_2Se_3 single crystal, with an inset photograph of the crystal as grown.

~88 cm^{-1}, which is missing in the 3R phase.[51,52] Transmission electron microscopy (TEM) characterization further supports this assignment (HR-TEM in Fig. 1c and small-area electron diffraction in Fig. 1d).

2.2 Surface chemical reactivity

To assess the oxidation resistance of α-In_2Se_3, we modelled the physisorption and the following decomposition of molecular oxygen (O_2) on different terminations of α-In_2Se_3. Firstly, we calculated the formation energies for Se vacancies. The formation of the single Se vacancy in the $InSe_2$ termination requires energies as high as 191 and 189 kJ mol^{-1} for bulk and monolayer, respectively. In the case of the InSe termination, the formation of the single Se vacancy corresponds to energy costs of 102 and 183 kJ mol^{-1} for bulk and monolayer, respectively. Therefore, the presence of Se vacancies appears to be unavoidable.

Calculations (see Table 1) indicate that in the absence of Se vacancies, adsorption and further decomposition of molecular oxygen would be energetically unfavorable even at zero temperature. Increasing temperature enhances the contribution from entropy, making the physisorption of molecular oxygen on defect-free α-In_2Se_3 less favorable. However, the presence of Se vacancies is crucial, as, in defective α-In_2Se_3, the physisorption and further chemical decomposition of oxygen molecules is an exothermic process for both terminations in bulk and in monolayer. The physisorption of molecular oxygen on Se vacancies is stable even at 400 °C. Similar calculations were performed for water adsorption on various surfaces of bulk and monolayer α-In_2Se_3, and results of the calculations (see Table 1) demonstrate that physical adsorption of water is stable only at Se vacancies in the InSe-terminated surface of bulk or monolayer α-In_2Se_3. Therefore, only some defective sites of bulk and monolayer α-In_2Se_3 will be oxidized, even after prolonged storage in ambient conditions.

To validate theoretical predictions on the chemical stability of α-In_2Se_3, we conducted near-ambient pressure X-ray photoelectron spectroscopy (NAP-XPS) experiments on bulk crystals exposed to O_2 and H_2O with a total dose of 10^{10} L (1 L = 10^{-6} Torr s). The Se-3d core level of the as-cleaved sample (Fig. 2) has a binding energy (BE) of ~55.0 eV, and a minor component related to Se(0) is present at BE of ~55.7 eV. The In-3d core levels (Fig. 2) exhibit a single peak with the $J = 5/2$ component located at BE = ~446 eV, congruent with previous reports for In_2Se_3.[53,54] Notably, exposure to 10^{10} L of oxygen and water did not cause any change in both In-3d and Se-3d core levels, indicating the superior oxidation resistance of bulk In_2Se_3.

2.3 In_2Se_3 nanosheets

To maximize surface area, we produced nanosheets of In_2Se_3 by liquid-phase exfoliation, with an average lateral size of ~450 nm (see the distribution in Fig. 3c) and an average thickness of ~15 nm (see the distribution in Fig. 3e). The selected area electron diffraction (SAED) pattern in Fig. 1d suggests a certain mosaicity around the [001] hexagonal axis, as indicated by the presence of elongated diffraction peaks. The six-fold symmetry of the HRTEM pattern corresponds to the [001] zone axis orientation, while the step-like grey contrast confirms the decreasing thickness, given by the diminishing number of overlapped structural foils towards the crystal border. The outermost border of the grain consists of a thin (~2.5 nm) amorphous layer, resulting from surface oxidation. Actually, the surface oxidation became relevant for the case of exfoliated nanosheets, because of the presence of vacancy sites, which promote surface oxidation, in agreement with the theoretical results in Table 1. We assessed the stability of exfoliated In_2Se_3 nanosheets by synchrotron-based X-ray photoemission electron microscopy (XPEEM), which allows the acquisition of XPS spectra with nanoscale spatial resolution. The binding energy of In-4d and Se-3d is ~18.2 and 54.3 eV (Fig. 3h), respectively, consistent with previous reports for In_2Se_3.[55,56] Additionally, the In-4d spectra have a secondary component located at ~18.5 eV related to indium oxide,[57–59] as highlighted in the HRTEM image in Fig. 3f.

2.4 Gas sensing with In_2Se_3 nanosheets

To assess the suitability of In_2Se_3 for gas sensing, we used DFT calculations. Firstly, we modelled physisorption of various analytes on the surfaces of bulk and monolayer α-In_2Se_3, with and without Se vacancies. Calculations (see Table 1) indicate that adsorption of molecular hydrogen is stable only at temperatures below 150 K, even at defect sites. At higher temperature, adsorption of H_2 on α-In_2Se_3 is metastable. The differential enthalpy of physisorption of water molecules is larger than for hydrogen molecule, especially for adsorption on Se vacancies. For example, the values for adsorption of H_2O and H_2 on Se vacancies in $InSe_2$ side of monolayer are −38.8 and −11.7 kJ mol^{-1}, respectively. However, at the temperatures used in sensing experiments (above 200 °C), adsorption of water is also metastable. Regarding CO and CO_2, their adsorption on α-In_2Se_3 surfaces is metastable at 200 °C and unstable at 300 °C. The differential Gibbs free energies for both CO and CO_2 were calculated to be above +10 kJ mol^{-1} for these temperatures. Notably, the physisorption of NO_2 exhibits a significantly different behaviour compared to other analyzed substances. Firstly, the differential enthalpy of adsorption of NO_2 is negative, even for defect-free substrates (as seen in Table 1), and its magnitude is larger than for the other considered analytes. This dissimilarity for NO_2 is related to the charge transfer between the analyte and substrate, with visible changes in the electronic structure and significant charge redistribution at the interface (as demonstrated in Fig. 4a and b). It is worth noting that even visible changes in charge densities (Fig. 4b) do not provide qualitative changes in the electronic structure in the vicinity of the Fermi energy (Fig. 4c).

The adsorption of NO_2 on α-In_2Se_3 is less stable with increasing temperature (the differential Gibbs free energy increases up to 11.1 kJ mol^{-1}). However, up to 300 °C, the adsorption of NO_2 on both terminations of bulk and monolayer of α-In_2Se_3 is stable on Se vacancies with differential Gibbs free energies below −50 kJ mol^{-1}, or metastable on defect-free regions. Further increasing of the temperature up to 400 °C

Table 1 Differential enthalpy and Gibbs free energies at different temperatures for various surface terminations of bulk/monolayer of α-In_2Se_3. Calculated energy costs of oxygen molecule decomposition are shown in parentheses. Negative values indicate exothermic processes, while positive values indicate endothermic processes

		ΔG [kJ mol^{-1}]		
Termination of α-In_2Se_3	ΔH [kJ mol^{-1}]	200 °C	300 °C	400 °C
O_2				
$InSe_2$	+11.1 (+136.9)/+91.3 (+52.7)	+29.3/+109.5	+33.2/+113.4	+37.0/+117.2
$InSe_{1.9}$	−102.6 (−108.1)/−173.9 (−213.6)	−84.4/−155.7	−80.5/−151.8	−76.7/−147.9
InSe	+6.6 (+40.9)/+18.6 (+125.4)	+24.8/+36.8	+28.7/+40.7	+32.5/+44.5
$InSe_{0.9}$	−68.8 (−61.9)/−0.4 (−86.2)	−50.6/+17.8	−46.7/+21.7	−42.8/+25.5
H_2O				
$InSe_2$	−10.3/−12.8	+39.4/+36.9	+49.9/+47.4	+60.4/+57.9
$InSe_{1.9}$	−21.3/−36.8	+28.6/+12.9	+38.9/+23.4	+50.4/+33.9
InSe	−13.1/−13.8	+36.6/+35.9	+47.1/+46.4	+57.6/+56.9
$InSe_{0.9}$	−60.9/−54.1	−11.2/−4.4	−0.2/+6.1	+9.8/+16.6
CO				
$InSe_2$	+14.2/−5.7	+31.9/+12.0	+51.4/+31.5	+57.9/+38.0
$InSe_{1.9}$	−22.4/−19.9	−4.7/−2.2	+ 14.8/+ 17.3	+ 21.3/+ 23.8
InSe	−9.5/−7.2	+8.2/+10.5	+27.7/+30.0	+34.2/+35.5
$InSe_{0.9}$	−44.3/−23.4	−26.6/−5.7	−7.1/+ 13.8	−0.6/+ 20.3
H_2				
$InSe_2$	−4.3/−5.0	+8.7/+8.0	+11.6/+10.9	+14.4/+13.7
$InSe_{1.9}$	+1.2/−11.7	+14.2/+1.3	+17.1/+4.2	+19.9/+7.0
InSe	+7.3/−5.0	+18.0/+8.0	+23.2/+10.9	+26.0/+13.7
$InSe_{0.9}$	−1.3/−0.5	+9.7/+10.5	+14.6/+15.4	+17.4/+18.2
CO_2				
$InSe_2$	−17.4/−3.2	+8.1/+22.3	+13.5/+27.7	+18.9/+33.1
$InSe_{1.9}$	−28.4/−23.4	−2.9/+ 2.1	+ 2.5/+ 7.5	+ 7.9/+12.9
InSe	−16.6/−2.7	+8.9/+22.8	+14.3/+28.2	+27.4/+33.6
$InSe_{0.9}$	−47.5/−23.4	−22.0/+ 2.1	−16.6/+ 7.5	−11.2/+12.9
NO_2				
$InSe_2$	−47.2/−31.3	+5.3/+21.2	+16.6/+32.3	27.5/+43.4
$InSe_2$ + H_2O	−71.7/−33.3	−19.2/+19.2	−8.1/+30.3	+3.0/+41.4
$InSe_{1.9}$	−111.3/−126.7	−58.8/−74.2	−47.7/−63.1	−36.5/−51.9
InSe	−40.3/−2.7	+40.2/+49.8	+20.3/+60.9	+34.4/+72.0
InSe + H $_2$O	−87.7/−139.2	−35.2/−86.7	−23.9/−75.4	−13.0/−64.5
$InSe_{0.9}$	−194.5/−120.5	−142.0/−68.0	−130.9/−56.9	−119.7/−45.7
$(CH_3)_2CO$ (acetone)				
$InSe_2$	−25.7/−25.3	+25.9/+26.3	+36.8/+37.2	+47.7/+48.1
$InSe_{1.9}$	−50.7/−57.3	+0.9/−5.7	+11.8/+5.2	+22.7/+16.1
InSe	+32.8/+29.6	+84.4/+81.2	+95.3/+92.1	+106.2/+103.0
$InSe_{0.9}$	−35.0/−58.8	+16.6/−7.2	+27.5/+3.7	+38.4/+14.6
C_2H_5OH (ethanol)				
$InSe_2$	−19.3/−17.7	+19.7/+21.3	+27.9/+29.5	+36.2/+37.8
$InSe_{1.9}$	−55.2/−57.2	−16.2/−18.2	−7.9/−10.0	+0.3/−1.7
InSe	−4.4/−20.6	+34.6/+18.4	+42.8/+26.6	+51.1/+34.9
$InSe_{0.9}$	−99.7/−136.7	−60.7/−97.7	−52.4/−89.5	−44.2/−81.2
NH_3				
$InSe_2$	+190.3/+183.1	+235.2/+228.0	+244.7/+237.5	+254.2/+247.0
$InSe_{1.9}$	−73.9/−74.1	−29.0/−29.2	−19.5/−19.7	−10.0/−10.2
InSe	−58.4/−57.7	−13.5/−12.8	−4.0/−3.3	+5.5/+6.2
$InSe_{0.9}$	−67.8/−77.5	−22.9/−32.6	−13.4/−23.1	−3.9/−13.6
H_2S				
$InSe_2$	−11.3/−13.3	+29.9/+27.3	+38.6/+36.6	+47.3/+44.3

Table 1 (*Contd.*)

Termination of α-In_2Se_3	ΔH [kJ mol^{-1}]	ΔG [kJ mol^{-1}]		
		200 °C	300 °C	400 °C
$InSe_{1.9}$	−36.3/−15.9	+4.9/+25.3	+13.6/+34.0	+22.3/+42.6
InSe	−25.6/−26.8	+15.6/+14.4	+24.3/+23.1	+33.0/+31.7
$InSe_{0.9}$	−67.8/−47.0	−26.6/−5.8	−17.9/+2.9	−9.3/+11.5

corresponds to stable adsorption of NO_2 only at Se vacancies. The calculated differential Gibbs free energies of the adsorption of NO_2 at 400 °C on Se vacancies in α-In_2Se_3 monolayers are −51.9 and −45.7 kJ mol^{-1} for $InSe_{1.9}$ and $InSe_{0.9}$ terminations, respectively.

In_2Se_3-based NO_2 gas sensors are designed to work in the ambient atmosphere, *i.e.*, in the presence of coadsorbed molecules, especially water (based on results in Table 1). Calculations for adsorption of NO_2 on defect-free surfaces of bulk and monolayer α-In_2Se_3 with pre-adsorbed single water molecule ($InSe_2$ + H_2O and InSe + H_2O in Table 1) indicate that pre-adsorption of water decreases the differential enthalpy of adsorption for all considered surfaces. In the presence of pre-adsorbed water, the differential Gibbs free energy of the adsorption of NO_2 on InSe-terminated surface of α-In_2Se_3 is negative even at 400 °C (−13.0 and −64.5 kJ mol^{-1} for bulk and monolayer, respectively). Moderate doping by pre-adsorbed water molecules increases the substrate's affinity for NO_2, which corresponds to a decrease of the differential enthalpy of adsorption. This contribution from charge transfer in the energetics of physisorption overcomes the energy cost of small distortions of the substrate (about 10 kJ per supercell), caused by the formation of non-covalent substrate-analyte bonds. A similar effect is also observed for both terminations of α-In_2Se_3.

As regards volatile organic compounds (VOC), calculations (Table 1) show that the adsorption of acetone and ethanol is more stable than hydrogen but less stable than nitrogen dioxide. Explicitly, the lowest values of the differential Gibbs free energy of the adsorption at 200 °C are −142.0 kJ mol^{-1} for NO_2, +0.9 kJ mol^{-1} for acetone, −60.7 kJ mol^{-1} for ethanol, −10.0 kJ mol^{-1} for NH_3, −9.3 kJ mol^{-1} for H_2S, and +8.7 kJ mol^{-1} for H_2. Notably, despite the larger size of ethanol and acetone, both molecules demonstrate preferential adsorption on Se vacancies. Thus, we can propose that, at higher temperatures, some minor amount of adsorbed NO_2 molecules leave adsorption sites (especially, Se vacancies). Subsequently, these sites could be occupied by VOC molecules, as well as by the molecules with small size and negative adsorption energy such as NH_3 and H_2S. The cause of this high selectivity to adsorption of the NO_2 on α-In_2Se_3 is the combination of the small size and the peculiar polarization of these molecules. Robust electrostatic interactions between negatively charged Se centres (see Fig. 4a and b) on the surface and positively charged nitrogen significantly decrease the differential enthalpy of the

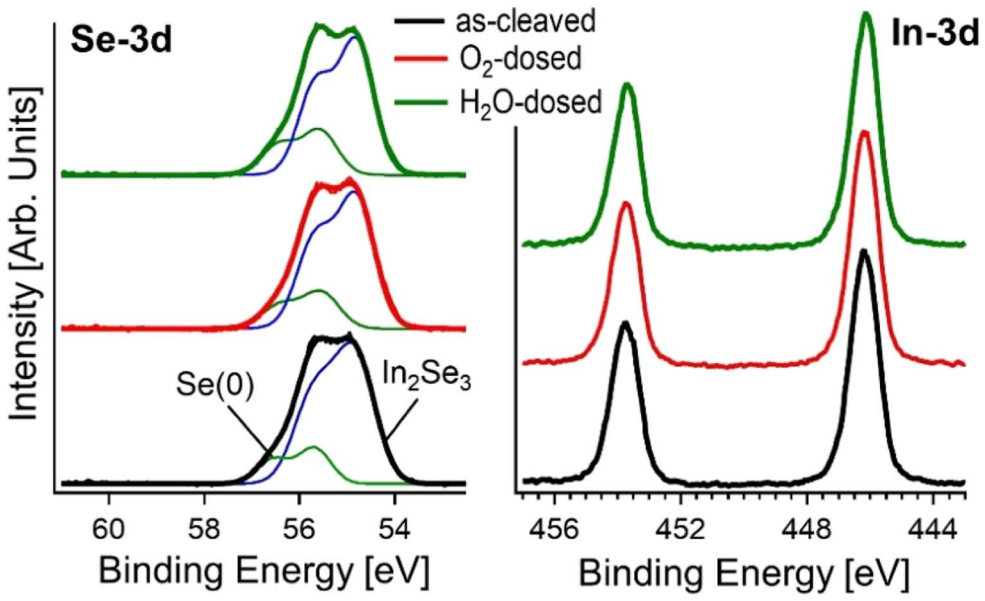

Fig. 2 X-ray photoelectron spectroscopy (XPS) spectra of Se-3d and In-3d core levels for the as-cleaved surface of the bulk crystal of α-In_2Se_3, and after exposure to 10^{10} L of O_2 and H_2O.

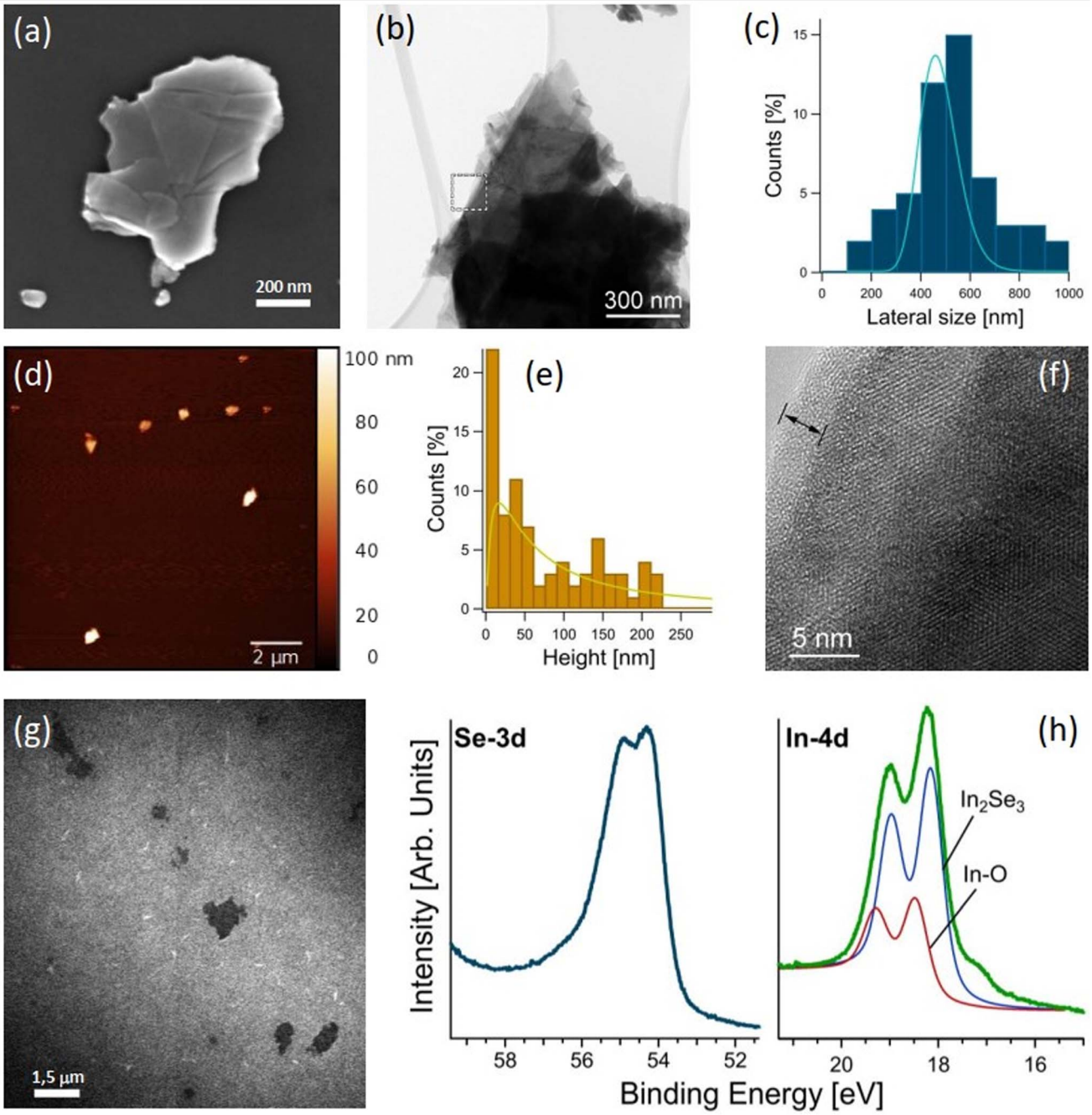

Fig. 3 Structural and morphological characterization of exfoliated In_2Se_3 nanosheets. (a) SEM and (b) TEM images showing the typical morphology of In_2Se_3 flakes. (c) Lateral size distribution obtained from a large dataset of SEM images. (d) AFM image of In_2Se_3 flakes showing their thickness. (e) Thickness distribution obtained from AFM measurements. (f) HRTEM image of a thin area at the edge of the nanosheet. (g) XPEEM image at the In-4d core level. (h) μ-XPS spectra in the region of Se-3d and In-4d core levels. Photon energy was 110 and 70 eV, respectively.

adsorption. The small size of NO_2 leads to a decrease of the energy cost of distortion of the substrate caused by the formation of non-covalent bonds, which is extremely important for the material with a peculiar surface structure. Contrarily, β-In_2Se_3 has a much more rigid surface and it has an inherently lower selectivity in the adsorption of reactants (see ESI, Table S3†).

Recently, other theoretical predictions have proposed In_2Se_3 as a suitable platform for gas sensing.[60,61] However, a careful inspection of these works evidences the presence of severe inconsistencies, which led to misleading conclusions. Specifically, in ref. 60, analyte adsorption was considered only at Se sites of the α-In_2Se_3 surface, which are usually unfavourable for adsorption. This led to calculated values of the differential enthalpies of adsorption that were positive and indicative of unstable adsorption. On the other hand, ref. 61 recognized more appropriate adsorption sites for CO, NO, and NO_2 on β-In_2Se_3, but claimed its superiority with respect to α-In_2Se_3 based

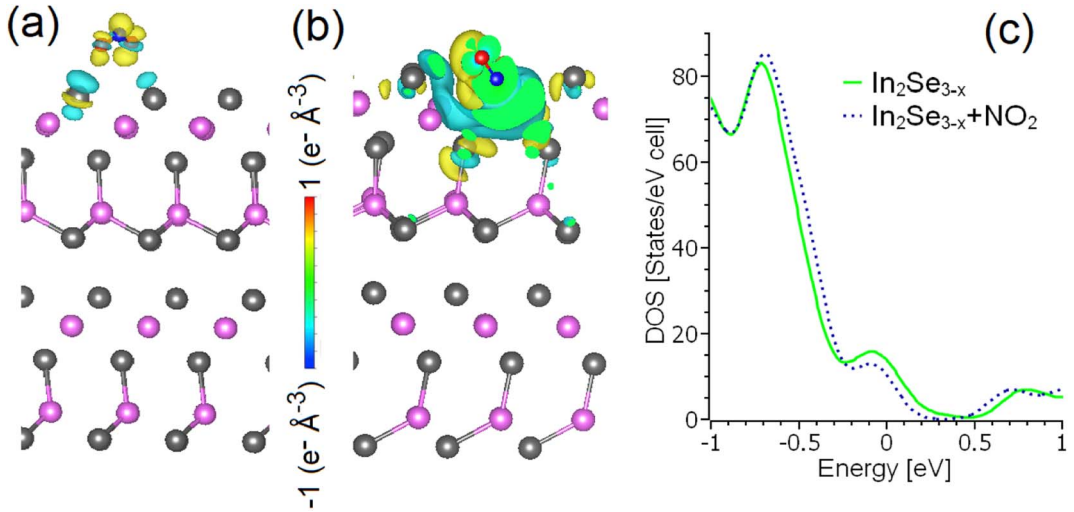

Fig. 4 Changes in the charge density distribution following the adsorption of NO_2 on the (a) $InSe_2$- and (b) $InSe_{1.9}$-terminated surfaces of α-In_2Se_3, along with (c) the total densities of states of α-In_2Se_{3-x} before and after physisorption of NO_2 on one Se vacancy in the $InSe_{1.9}$-terminated surface.

on the incorrect choice of adsorption sites in ref. 60. Additionally, the reported (i) adsorption energies, (ii) charge transfers, and (iii) changes in electronic structure for CO and NO_2 on β-In_2Se_3 in ref. 61 are rather close. To resolve the issue related to the presence of controversial reports, systematic calculations for adsorption of species under consideration were carried out for both bulk and monolayer β-In_2Se_3. Results of the calculations (see ESI, Table S3†) demonstrate that even at 400 °C stable adsorption of H_2S, NH_3, ethanol, acetone, CO, and CO_2 should occur even on defects-free surfaces of β-In_2Se_3. Accordingly, β-In_2Se_3 cannot be considered neither as CO-tolerant nor as material sensitive to some special compounds.[60,61]

Theoretical results on gas sensing were validated by tests after having fabricated gas sensors, following methods discussed in the corresponding section. Fig. 5a reports the response of α-In_2Se_3 towards 1 ppm of NO_2 at the operating temperatures of 100–400 °C. The response values of the material were calculated as the relative variation of its electrical resistance (eqn (1)), where R_0 is the baseline resistance value of the sensor in air, and R_f is the steady state value of its resistance in the presence of NO_2 gas.

$$S = \frac{(R_f - R_0)}{R_0} = \frac{\Delta R}{R_0} \quad (1)$$

Fabricated α-In_2Se_3 sensors had a high response ($S = 73.0$) to NO_2 at 200 °C, with a slightly higher response ($S = 73.7$) at 250 °C. However, the sensing response of α-In_2Se_3 decreased with increasing operating temperature, reaching its lowest value ($S = 2.7$) at 400 °C. These experimental findings were consistent with the DFT calculations, which indicated that the adsorption of NO_2 on α-In_2Se_3 was stable at Se vacancies and metastable at defect-free zones at ≤300 °C, while it was stable only at Se vacancies at an operating temperature of 400 °C. Moreover, we found that the conductance of α-In_2Se_3 did not fully recover to its baseline after the gas sensing tests at 200 and 250 °C.

We also measured the conductance variation associated with the exposure to different concentrations of NO_2 and found a reversible sensing response at 300 °C (Fig. 5b). Specifically, NO_2 as an oxidizing gas was adsorbed on the surface of α-In_2Se_3, trapping electrons from its surface and reducing the density of charge carriers, leading to a reduction of the conductance of the sensing structure. The temperature increase to 300 °C enhanced the desorption of NO_2, ensuring the recovery of the sensor conductance to its baseline value. Therefore, the optimal operating temperature of α-In_2Se_3-based sensors was 300 °C. Table S1 in the ESI† reports the response of the material to different concentrations of NO_2 at 300 °C. Furthermore, the conductance reduction of the structure after the injection of each concentration of NO_2 into the test chamber and its recovery to the initial stage (Fig. 5b) indicated the n-type sensing behavior of α-In_2Se_3. The response variation of the fabricated sensor depending on the concentration of NO_2 (Fig. 5c) indicated that α-In_2Se_3 was suitable for providing quantification analysis of the analyte gas.

Moreover, α-In_2Se_3 displays high sensitivity ($S = 9.8$) towards 200 ppb of NO_2, which is particularly significant, considering the health risks associated with short-term exposure to NO_2 gas. Based on research findings, the occupational exposure limit for NO_2 gas should not exceed 5 ppm.[62] Our study highlights the critical sensitivity of α-In_2Se_3-based sensors to low concentrations of NO_2, making it a promising candidate for real-life applications. To estimate the limit of detection (LOD) of the α-In_2Se_3 sensor, we used a power law function to fit the experimental data (ESI, Fig. S1b†). The LOD for the structure is approximately 5 ppb ± 5%.

The humidity level is another crucial factor that can affect the functionality of chemiresistive gas sensors. Therefore, we investigated the electrical and sensing properties of α-In_2Se_3 at

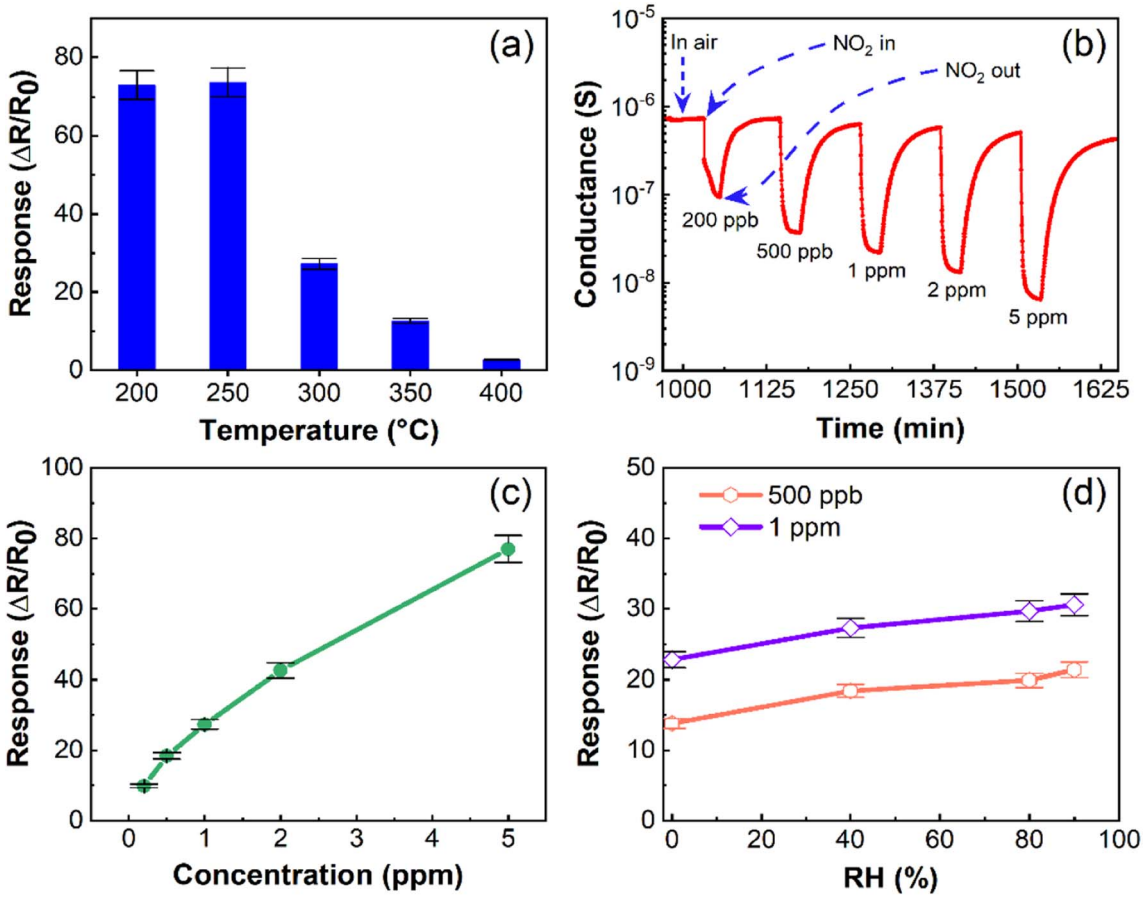

Fig. 5 Gas sensing performance of α-In_2Se_3. (a) Response of α-In_2Se_3 to 1 ppm NO_2 as a function of operating temperature (RH = 40% in the test chamber). (b) Dynamic response of α-In_2Se_3 to different concentrations of NO_2 (200 ppb to 5 ppm) at 300 °C. (c) Response of α-In_2Se_3 to NO_2 concentrations ranging from 0.2 to 5.0 ppm at an operating temperature of 300 °C. (d) Response of α-In_2Se_3 to 500 ppb and 1 ppm NO_2 at various humidity levels (dry air, 40%, 60%, 80%, and 90% RH).

its optimal operating temperature under varying relative humidity (RH) levels in the test chamber. The conductance behavior at 300 °C, as shown in Fig. S1a in the ESI,† indicates that the conductance is slightly higher at 40% RH compared to dry air conditions. However, significant variations were not observed at higher RH levels (40–90%). Fig. 5d displays the response of α-In_2Se_3 towards 500 ppb and 1 ppm of NO_2 as a function of RH concentration. As RH increased from 0 (dry air) to 40% in the test chamber, the response towards 500 ppb and 1 ppm of NO_2 increased by 25% and 17%, respectively. At 90% RH, the response towards 500 ppb and 1 ppm of NO_2 was 14% and 11% higher than at 40% RH, respectively. These results suggest that α-In_2Se_3 exhibits stable electrical and sensing performance at different RH levels, particularly in the range of 40–90%, corresponding to real-life conditions. These slight variations in the response of the sensor to increasing the concentration of RH in the chamber are due to the dissociation of water molecules on the surface of the sensing material resulting in the formation of hydroxyl groups, which may provide additional electrons.[63] However, the co-adsorption of water molecules and other gaseous compounds on a semiconductor is a complex mechanism and varied depending on the working conditions of the sensor. Furthermore, at relatively high operating temperatures the effect of water molecules is reduced due to their evaporation.[64]

It is also worth noting that our theoretical model predicts that water molecule adsorption on the material is metastable above 200 °C (Table 1). Therefore, the weak enhancement in electrical conductance and sensor response at high RH levels aligns with theoretical predictions.

To evaluate the performance for NO_2 sensing, we compared α-In_2Se_3 with other sensors based on 2D semiconductors (SnS_2,[65] Sb_2Se_3,[66] N-doped In_2S_3,[67] black phosphorus,[68] reduced graphene oxide[69]), graphitic carbon nitride,[70] metal oxides (In_2O_3 nanoparticles,[71,72] SnO_2 nanowires[73]), and various heterostructures (SnO_2/$SnSe_{1.7}$,[74] In_2O_3/SnS_2,[75] SnO_2/SnS_2,[76] $SnSe_2$/SnO/SnSe,[77] In_2O_3 nanoparticles/SnO_2 nanowires[73]). The comparative analysis highlights the superior suitability of α-In_2Se_3 compared to state-of-the-art materials, with significantly higher sensing response and lower LOD than all other above-mentioned systems. Additionally, while water adsorption is unfavorable on α-In_2Se_3 surfaces, it is energetically favorable at near-room temperature on the surfaces of all other above-mentioned systems, leading to detrimental effects on their gas-sensing properties.

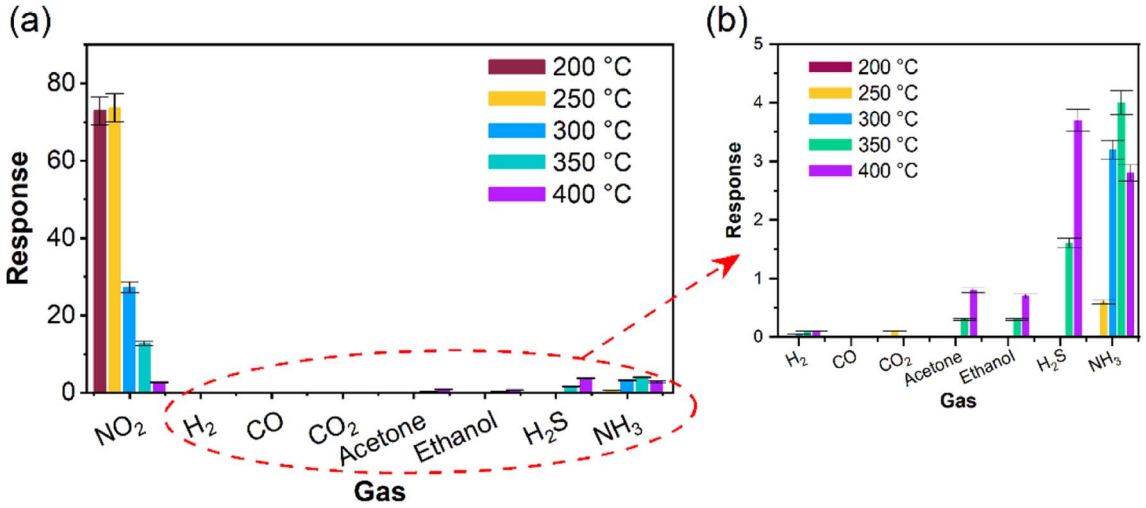

Fig. 6 Gas sensing performance of α-In_2Se_3. (a) Response of the material to 1 ppm of NO_2, 25 ppm of H_2 and CO, 5 ppm of acetone and ethanol at temperatures, 2 ppm of H_2S and 5 ppm of NH_3 ranging from 200 to 400 °C. (b) Magnified section of panel (a), showing the response values of α-In_2Se_3 towards H_2, CO, acetone, and ethanol.

To ensure that α-In_2Se_3-based sensors are selective towards the target gas (NO_2) and not affected by other interfering gases, we investigated the selectivity of α-In_2Se_3 towards different gaseous and volatile organic compounds. Fig. 6 illustrates the response of the material to NO_2, H_2, CO, $(CH_3)_2CO$ (acetone), C_2H_5OH (ethanol), H_2S, and NH_3 at the operating temperatures of 200–400 °C. The response value towards reducing gases was calculated using eqn (2), where G_0 is the conductance of α-In_2Se_3 in air and G_f is the steady-state value of sensor conductance in the presence of gas.

$$\frac{(G_f - G_0)}{G_0} = \frac{\Delta G}{G_0} \quad (2)$$

α-In_2Se_3 exhibited an excellent selective response to NO_2. Moreover, the material was found to be insensitive to 25 ppm of CO, 800 ppm of CO_2, 2 ppm of H_2S, and 5 ppm of acetone and ethanol, it had a very weak response (0.06) to 25 ppm of H_2 and a significantly lower response value (3.2) to 5 ppm of NH_3 compared to the 1 ppm of NO_2 (27.3) at its optimum operating temperature of 300 °C.

It is worth noting that H_2, acetone, ethanol, H_2S, and NH_3 adsorption induced small changes in the electronic structure of the material, while CO_2 caused a weak change at relatively low temperatures and CO did not affect the electronic structure of the sensor. However, the NO_2 sensing response of the material was remarkably high, owing to the negative differential enthalpy of the adsorption of NO_2 and the larger magnitude of the enthalpy of NO_2 adsorption compared to other gaseous and volatile compounds (as shown in Table 1). This exceptional selective response is attributed to the strongest binding energy for NO_2. Our theoretical simulations are consistent with the experimental results, supporting our findings. Moreover, the gas sensing tests after two months show that the α-In_2Se_3 has stable performance for the detection of NO_2 (ESI, Fig. S2†). For the sake of completeness, we also report in ESI, Fig. S3† the conductance as a function of time dependence for In_2Se_3-based sensors at 300 °C.

3 Conclusions

In summary, our study has successfully demonstrated the exceptional sensing performance of In_2Se_3 nanosheets towards NO_2 gas. The material exhibits high selectivity and sensitivity to NO_2, with a LOD of only 5 ppb at an operating temperature of 300 °C. The theoretical simulations and experimental measurements indicate that the unique selectivity of In_2Se_3 towards NO_2 is attributed to the negative differential enthalpy of NO_2 adsorption, as well as the larger magnitude of the enthalpy of NO_2 adsorption compared to other gases and VOC.

We also found that the interaction between the In_2Se_3 and H_2, acetone, ethanol, CO, and CO_2 is metastable at high operating temperatures. NO_2 is stably adsorbed on the In_2Se_3 nanosheets even at high temperatures, especially on Se vacancies. Furthermore, theoretical simulations demonstrate that the chemical properties of In_2Se_3 are independent of the number of layers and termination of the surface, indicating its scalability and potential for practical applications.

The stability of In_2Se_3 towards oxidation and CO-poisoning was also confirmed by XPS measurements and theoretical simulations. The scalability and stability of the material towards oxidation and CO-poisoning, as well as its unique selectivity towards NO_2, suggest that it could be used in gas detection systems for harsh environments, such as industrial settings, where other gas sensors may fail. Additionally, our sensors are highly scalable due to the solution-based processing approach, which enables the fabrication of large-area devices, making them ideal for practical gas sensing applications, as an example for the development of complex composite nanostructured sensors. We anticipate that our findings will

contribute to the advancement of gas sensing technology and inspire further studies on In_2Se_3 and related materials. The various unique features of In_2Se_3-based sensors could potentially open up new opportunities for the development of gas sensing devices with tailored properties.

4 Methods

4.1 Single-crystal growth

In_2Se_3 single crystals were grown by a chemical vapor transport method. In pieces (99.99%) and Se pellets (99.99%) in a stoichiometric ratio of 2 : 3 with additional iodine (99.9%, 5 mg cm^{-3}) were sealed in an evacuated silica ampoule (170 mm in length and 16 mm in inner diameter). Then, the ampoule was heated in a two-zone tubular furnace. The reactant zone was slowly heated up (~12 h) to 900 C, while the other end was set to 750 C. The entire growth process was maintained for 300 h, followed by a naturally cooling process down to room temperature. Black plate-like crystals with typical dimensions of 5 × 5 × 0.03 mm^3. The crystal structure was characterized using powder XRD (Bruker D2) with Cu-Kα radiation. The single crystal quality and crystallization directions were identified by the Laue diffraction method (Photonic Science).

4.2 Liquid-phase exfoliation and production of nanosheets

To produce a fine powder, In_2Se_3 crystals were meticulously ground using a mortar. Following this, 0.03 grams of the resulting In_2Se_3 powder were dispersed in 10 milliliters of isopropyl alcohol (IPA). This dispersion was then subjected to a three-hour sonication process in a temperature-controlled bath sonicator, ensuring that the temperature remained below 20 °C. After sonication, the sample underwent centrifugation at 1000 rpm, effectively separating the exfoliated flakes from any unexfoliated material. Finally, the supernatant was collected and prepared for subsequent analysis.

4.3 Fabrication and characterization of sensors

Al_2O_3 substrates with dimensions of 2 mm × 2 mm × 0.75 mm were cleaned in acetone and ethanol using an ultrasonic bath and then were washed with distilled water. Platinum (Pt) interdigitated electrodes (ESI, Fig. S4†) were deposited on the surface of the substrates using radiofrequency (13.56 MHz) magnetron sputtering for electrical measurements. To perform sensing characterization of the prepared α-In_2Se_3 layers at different operating temperatures, a Pt meander was deposited on the backside of the Al_2O_3 substrates as a heater. To perform the sensing measurements, a flow-through system was used, where a stream of synthetic air/analyte gas mixture (constant flow, 0.3 L min^{-1}) passed through the test chamber. The level of RH in the chamber during the measurements was kept under the control using a humidity sensor. A detailed description of the configuration of the chemoresistive sensing device and gas test system was reported in our previous works.[78,79]

In_2Se_3 layers were dispersed in isopropanol at a concentration of 3 mg mL^{-1}. The prepared dispersion was drop cast on the surface of Al_2O_3 substrates. A high-precision dispenser (Gilson Company, Inc, USA) was used for drop casting. The electrical conductance of the fabricated sensors was stabilized at each operating temperature for 10 h, and then the analyte gas with the desired concentration was injected into the test chamber. The conductance value of the sensing structures was monitored by the volt–amperometric method. The applied voltage for the measurements was 1 V.

4.4 TEM

Sample was prepared for TEM experiments by dripping a liquid suspension containing α-In_2Se_3 nanosheets onto the TEM grid, provided with a lacey carbon membrane. Experiments were carried out a JEM ARM200F TEM operating at 200 kV.

4.5 XPS

A NAP-XPS apparatus at the Charles University in Prague, Czech Republic, equipped with a Scienta R3000 hemispherical electron analyzer and Al K_α X-ray source, was used for *in situ* measurements for bulk crystals exposed to gases in NAP conditions.

The XPEEM measurement took place at the PEEM endstation within the MAXPEEM Beamline at MAX IV Laboratory in Lund, Sweden. The sample was prepared through drop casting and subsequently dried in an ultra-high vacuum (UHV) environment for 4 hours at 350 °C. The experiment utilized a linearly polarized photon beam at perpendicular incidence angles. No beam-induced damage was observed throughout the process.

4.6 DFT calculations

The atomic structure, energetics of various configurations, and interactions were studied by DFT using the QUANTUM-ESPRESSO code[80] with GGA–PBE,[81] taking into account van der Waals-like forces correction.[82] Ultrasoft pseudopotentials[83] were used for all simulations, with energy cutoffs of 55 and 400 Ry for the plane-wave expansion of the wave functions and the charge density, respectively. Physisorption enthalpies were also calculated by the standard formula:

$$\Delta H_{\text{phys}} = [E_{\text{subst+mol}} - (E_{\text{subst}} + E_{\text{mol}})],$$

where E_{subst} is the total energy of the substrate and E_{mol} is the energy of the single molecules of the selected species in an empty box. In the case of water adsorption, only the gaseous phase was considered. Decomposition energy was defined as the difference between the total energy of the system with an adsorbed molecule and the total energy of same system after decomposition on the surface. For physisorption, the differential Gibbs free energy at given temperature was also evaluated using the formula:

$$\Delta G = \Delta H - T\Delta S,$$

where T is the temperature and ΔS is the change of entropy of the adsorbed molecule. The change in entropy ΔS was

estimated considering the gas → liquid transition using the standard formula:

$$\Delta S = \Delta H_{\text{vaporisation}}/T,$$

where $\Delta H_{\text{vaporization}}$ is the measured enthalpy of vaporization.

To test the technical parameters, we performed an optimization of the atomic structure of bulk In_2Se_3. Good convergence between the theoretical end experimental lattice parameters was achieved only for a rather large value of the energy cut-off. For simulations of the surface of the bulk crystal and monolayer, we used a 3×3 supercell. For the simulation of the bulk, we used an α-In_2Se_3 bilayer with fixed lattice parameters obtained in the calculations for bulk. Only atomic positions were optimized. This type of calculation imitates the effect of the rigid sub-surface bulk part of the crystal on the structure and properties of surface layers. To simulate a flexible monolayer, optimization of the lattice parameters and atomic positions was performed.

Conflicts of interest

There are no conflicts to declare.

Acknowledgements

The authors are grateful to Jessica Occhiuzzi for liquid-phase exfoliation. AP thanks CERIC-ERIC and NFFA-Europe for the access to NAP-XPS, XPEEM and HRTEM facilities. The simulations have been supported by High Performance Computing Platform of Nanjing University of Aeronautics and Astronautics. DWB acknowledges research funding from Jiangsu Innovative and Entrepreneurial Talents Project. CG and MCI acknowledge funding from the Ministry of Research, Innovation and Digitization (Romania) through contract POC No. 332/390008/29.12.2020-SMIS 109522.

References

1 W. H. Deng, L. He, E. X. Chen, G. E. Wang, X. L. Ye, Z. H. Fu, Q. Lin and G. Xu, *J. Mater. Chem. A*, 2022, **10**, 12977–12983.
2 X. Tian, L. Yao, X. Cui, R. Zhao, T. Chen, X. Xiao and Y. Wang, *J. Mater. Chem. A*, 2022, **10**, 5505–5519.
3 T. Wang, J. Liu, Y. Zhang, Q. Liang, R. Wu, H. S. Tsai, Y. Wang and J. Hao, *J. Mater. Chem. A*, 2022, **10**, 4306–4315.
4 R. Zhao, Y. Luo, F. Jiang, Y. Dai, Z. Ma, J. Zhong, P. Wu, T. Zhou and Y. Huang, *J. Mater. Chem. A*, 2022, **10**, 7948–7959.
5 C. Zhu, X. Dong, C. Guo, L. Huo, S. Gao, Z. Zheng, X. Cheng and Y. Xu, *J. Mater. Chem. A*, 2022, **10**, 12150–12156.
6 S. H. Kim, Y. K. Moon, J. H. Lee, Y. Chan Kang and S. Y. Jeong, *J. Mater. Chem. A*, 2022, **11**, 1159–1169.
7 Y. K. Moon, J. H. Kim, S. Y. Jeong, S. M. Lee, S. J. Park, T. H. Kim, J. H. Lee and Y. C. Kang, *J. Mater. Chem. A*, 2022, **11**, 666–675.
8 J. Yan, X. Guo, Y. Zhu, Z. Song and L. Y. S. Lee, *J. Mater. Chem. A*, 2022, **10**, 15657–15664.
9 Q. Hu, C. Wu, Z. Dong, G. Zhang, Z. Ma, X. Wang, S. Sun and J. Xu, *J. Mater. Chem. A*, 2022, **10**, 2786–2794.
10 Y. Yao, Y. Han, M. Zhou, L. Xie, X. Zhao, Z. Wang, N. Barsan and Z. Zhu, *J. Mater. Chem. A*, 2022, **10**, 8283–8292.
11 J. W. Baek, Y. H. Kim, J. Ahn, D. H. Kim, H. Shin, J. Ko, S. Park, C. Park, E. Shin, J. S. Jang and I. D. Kim, *J. Mater. Chem. A*, 2022, **10**, 23282–23293.
12 J. Fan, J. Gao, H. Lv, L. Jiang, F. Qin, Y. Fan, B. Sun, J. Wang, M. Ikram and K. Shi, *J. Mater. Chem. A*, 2022, **10**, 25714–25724.
13 X. Guo, Y. Shi, Y. Ding, Y. He, B. Du, C. Liang, Y. Tan, P. Liu, X. Miao, Y. He and X. Yang, *J. Mater. Chem. A*, 2022, **10**, 22629–22637.
14 K. Haddad, A. Abokifa, S. An, J. Lee, B. Raman, P. Biswas and J. D. Fortner, *J. Mater. Chem. A*, 2022, **11**, 447–459.
15 P. Qin, S. Okur, Y. Jiang and L. Heinke, *J. Mater. Chem. A*, 2022, **10**, 25347–25355.
16 B. Y. Song, C. Li, X. F. Zhang, R. Gao, X. L. Cheng, Z. P. Deng, Y. M. Xu, L. H. Huo and S. Gao, *J. Mater. Chem. A*, 2022, **10**, 14411–14422.
17 R. Wu, T. Xin, Y. Wang, T. Wang, L. Liu and J. Hao, *J. Mater. Chem. A*, 2022, **10**, 14810–14819.
18 S. Yu, J. Dong, H. Wang, S. Li, H. Zhu and T. Yang, *J. Mater. Chem. A*, 2022, **10**, 25453–25462.
19 L. Ju, X. Tan, X. Mao, Y. Gu, S. Smith, A. Du, Z. Chen, C. Chen and L. Kou, *Nat. Commun.*, 2021, **12**, 5128.
20 T. Tang, Z. Li, Y. F. Cheng, H. G. Xie, X. X. Wang, Y. L. Chen, L. Cheng, Y. Liang, X. Y. Hu and C. M. Hung, *J. Hazard. Mater.*, 2023, **451**, 131184.
21 Y. Cheng, Z. Li, T. Tang, K. Xu, H. Yu, X. Tao, C. M. Hung, N. D. Hoa, Y. Fang and B. Ren, *Appl. Mater. Today*, 2022, **26**, 101355.
22 R. Souissi, N. Bouguila, M. Bendahan, T. Fiorido, K. Aguir, M. Kraini, C. Vázquez-Vázquez and A. Labidi, *Sens. Actuators, B*, 2020, **319**, 128280.
23 P. Miro, M. Audiffred and T. Heine, *Chem. Soc. Rev.*, 2014, **43**, 6537–6554.
24 W. Zheng, X. Liu, J. Xie, G. Lu and J. Zhang, *Coord. Chem. Rev.*, 2021, **447**, 214151.
25 R. B. Jacobs-Gedrim, M. Shanmugam, N. Jain, C. A. Durcan, M. T. Murphy, T. M. Murray, R. J. Matyi, R. L. Moore and B. Yu, *ACS Nano*, 2014, **8**, 514–521.
26 W. Feng, F. Gao, Y. Hu, M. Dai, H. Li, L. Wang and P. Hu, *Nanotechnology*, 2018, **29**, 445205.
27 D. Kang, T. Rim, C. K. Baek, M. Meyyappan and J. S. Lee, *Small*, 2014, **10**, 3795–3802.
28 G. Han, Z.-G. Chen, J. Drennan and J. Zou, *Small*, 2014, **10**, 2747–2765.
29 Z. Zheng, J. Yao, B. Wang, Y. Yang, G. Yang and J. Li, *ACS Appl. Mater. Interfaces*, 2017, **9**, 43830–43837.
30 W. Feng, F. Gao, Y. Hu, M. Dai, H. Liu, L. Wang and P. Hu, *ACS Appl. Mater. Interfaces*, 2018, **10**, 27584–27588.
31 J. O. Island, S. I. Blanter, M. Buscema, H. S. van der Zant and A. Castellanos-Gomez, *Nano Lett.*, 2015, **15**, 7853–7858.
32 S. H. Kwon, B. T. Ahn, S. K. Kim, K. H. Yoon and J. Song, *Thin Solid Films*, 1998, **323**, 265–269.

33 A. M. Rasmussen, S. T. Teklemichael, E. Mafi, Y. Gu and M. D. McCluskey, *Appl. Phys. Lett.*, 2013, **102**, 062105.
34 Y.-T. Huang, C.-W. Huang, J.-Y. Chen, Y.-H. Ting, K.-C. Lu, Y.-L. Chueh and W.-W. Wu, *ACS Nano*, 2014, **8**, 9457–9462.
35 W. Ding, J. Zhu, Z. Wang, Y. Gao, D. Xiao, Y. Gu, Z. Zhang and W. Zhu, *Nat. Commun.*, 2017, **8**, 1–8.
36 C. Cui, W.-J. Hu, X. Yan, C. Addiego, W. Gao, Y. Wang, Z. Wang, L. Li, Y. Cheng, P. Li, X. Zhang, H. N. Alshareef, T. Wu, W. Zhu, X. Pan and L.-J. Li, *Nano Lett.*, 2018, **18**, 1253–1258.
37 Y. Zhou, D. Wu, Y. Zhu, Y. Cho, Q. He, X. Yang, K. Herrera, Z. Chu, Y. Han, M. C. Downer, H. Peng and K. Lai, *Nano Lett.*, 2017, **17**, 5508–5513.
38 J. Zhou, Q. Zeng, D. Lv, L. Sun, L. Niu, W. Fu, F. Liu, Z. Shen, C. Jin and Z. Liu, *Nano Lett.*, 2015, **15**, 6400–6405.
39 M. Balkanski, C. Julien, A. Chevy and K. Kambas, *Solid State Commun.*, 1986, **59**, 423–427.
40 X. Tao and Y. Gu, *Nano Lett.*, 2013, **13**, 3501–3505.
41 C. Amory, J. C. Bernède and S. Marsillac, *J. Appl. Phys.*, 2003, **94**, 6945–6948.
42 Y. Li, J. Gao, Q. Li, M. Peng, X. Sun, Y. Li, G. Yuan, W. Wen and M. Meyyappan, *J. Mater. Chem.*, 2011, **21**, 6944–6947.
43 A. Pfitzner and H. Lutz, *J. Solid State Chem.*, 1996, **124**, 305–308.
44 R. Vilaplana, S. G. Parra, A. Jorge-Montero, P. Rodríguez-Hernández, A. Munoz, D. Errandonea, A. Segura and F. J. Manjón, *Inorg. Chem.*, 2018, **57**, 8241–8252.
45 M. Küpers, P. M. Konze, A. Meledin, J. Mayer, U. Englert, M. Wuttig and R. Dronskowski, *Inorg. Chem.*, 2018, **57**, 11775–11781.
46 Y. Yin, Y. Zhang, T. Gao, T. Yao, X. Zhang, J. Han, X. Wang, Z. Zhang, P. Xu and P. Zhang, *Adv. Mater.*, 2017, **29**, 1700311.
47 Y. Yu, G.-H. Nam, Q. He, X.-J. Wu, K. Zhang, Z. Yang, J. Chen, Q. Ma, M. Zhao and Z. Liu, *Nat. Chem.*, 2018, **10**, 638–643.
48 A. Woolley and G. Wexler, *J. Phys. C: Solid State Phys.*, 1977, **10**, 2601.
49 A. Feroze, H. R. Na, Y. C. Park, J.-H. Jun, M.-H. Jung, J.-H. Lee, J.-H. Kim, M.-J. Seong, S. Hong and S.-H. Chun, *Cryst. Growth Des.*, 2020, **20**, 2860–2865.
50 J. Cui, L. Wang, Z. Du, P. Ying and Y. Deng, *J. Mater. Chem. C*, 2015, **3**, 9069–9075.
51 L. Liu, J. Dong, J. Huang, A. Nie, K. Zhai, J. Xiang, B. Wang, F. Wen, C. Mu, Z. Zhao, Y. Gong, Y. Tian and Z. Liu, *Chem. Mater.*, 2019, **31**, 10143–10149.
52 F. Xue, J. Zhang, W. Hu, W.-T. Hsu, A. Han, S.-F. Leung, J.-K. Huang, Y. Wan, S. Liu, J. Zhang, J.-H. He, W.-H. Chang, Z. L. Wang, X. Zhang and L.-J. Li, *ACS Nano*, 2018, **12**, 4976–4983.
53 C.-H. Ho, C.-H. Lin, Y.-P. Wang, Y.-C. Chen, S.-H. Chen and Y.-S. Huang, *ACS Appl. Mater. Interfaces*, 2013, **5**, 2269–2277.
54 Y. Jiang, Q. Wang, L. Han, X. Zhang, L. Jiang, Z. Wu, Y. Lai, D. Wang and F. Liu, *Chem. Eng. J.*, 2019, **358**, 752–758.
55 G. D'Olimpio, S. Nappini, M. Vorokhta, L. Lozzi, F. Genuzio, T. O. Mentes, V. Paolucci, B. Gurbulak, S. Duman, L. Ottaviano, A. Locatelli, F. Bondino, D. W. Boukhvalov and A. Politano, *Adv. Funct. Mater.*, 2020, **30**, 2005466.
56 I. N. Reddy, C. Venkata Reddy, M. Cho, J. Shim and D. Kim, *Mater. Res. Express*, 2017, **4**, 086406.
57 Z. M. Detweiler, S. M. Wulfsberg, M. G. Frith, A. B. Bocarsly and S. L. Bernasek, *Surf. Sci.*, 2016, **648**, 188–195.
58 A. Kyndiah, A. Ablat, S. Guyot-Reeb, T. Schultz, F. Zu, N. Koch, P. Amsalem, S. Chiodini, T. Yilmaz Alic, Y. Topal, M. Kus, L. Hirsch, S. Fasquel and M. Abbas, *Sci. Rep.*, 2018, **8**, 10946.
59 P.-H. Ho, Y.-R. Chang, Y.-C. Chu, M.-K. Li, C.-A. Tsai, W.-H. Wang, C.-H. Ho, C.-W. Chen and P.-W. Chiu, *ACS Nano*, 2017, **11**, 7362–7370.
60 Z. Xie, F. Yang, X. Xu, R. Lin and L. Chen, *Front. Chem.*, 2018, **6**, 430.
61 S. O. Bolarinwa, S. Sattar and A. A. AlShaikhi, *Comput. Mater. Sci.*, 2022, **201**, 110880.
62 M. I. Gilmour, P. Park and M. K. Selgrade, *Fundam. Appl. Toxicol.*, 1996, **31**, 65–70.
63 R. Pohle, M. Fleischer and H. Meixner, *Sens. Actuators, B*, 2000, **68**, 151–156.
64 E. Traversa, *Sens. Actuators, B*, 1995, **23**, 135–156.
65 M. Cheng, Z. Wu, G. Liu, L. Zhao, Y. Gao, B. Zhang, F. Liu, X. Yan, X. Liang, P. Sun and G. Lu, *Sens. Actuators, B*, 2019, **291**, 216–225.
66 Y. B. Kim, S. H. Jung, D. S. Kim, N. G. Deshpande, H. W. Suh, H. H. Lee, J. H. Choi, H. S. Lee and H. K. Cho, *Adv. Funct. Mater.*, 2021, **31**, 2102439.
67 Y. Cheng, Z. Li, T. Tang, K. Xu, H. Yu, X. Tao, C. M. Hung, N. D. Hoa, Y. Fang, B. Ren, H. Chen and J. Z. Ou, *Appl. Mater. Today*, 2022, **26**, 101355.
68 G. Lee, S. Kim, S. Jung, S. Jang and J. Kim, *Sens. Actuators, B*, 2017, **250**, 569–573.
69 S. Cui, H. Pu, E. C. Mattson, Z. Wen, J. Chang, Y. Hou, C. J. Hirschmugl and J. Chen, *Anal. Chem.*, 2014, **86**, 7516–7522.
70 A. Govind, P. Bharathi, G. Mathankumar, M. K. Mohan, J. Archana, S. Harish and M. Navaneethan, *Diamond Relat. Mater.*, 2022, **128**, 109205.
71 P. Sowti khiabani, E. Marzbanrad, H. Hassani and B. Raissi, *J. Am. Ceram. Soc.*, 2013, **96**, 2493–2498.
72 S. Shah, S. Han, S. Hussain, G. Liu, T. Shi, A. Shaheen, Z. Xu, M. Wang and G. Qiao, *Ceram. Int.*, 2022, **48**, 12291–12298.
73 S. Park, Y. W. Jung, G. M. Ko, D. Y. Jeong and C. Lee, *Appl. Phys. A*, 2021, **127**, 898.
74 V. Paolucci, G. D'Olimpio, C.-N. Kuo, C. S. Lue, D. W. Boukhvalov, C. Cantalini and A. Politano, *ACS Appl. Mater. Interfaces*, 2020, **12**(30), 34362–34369.
75 Y. Yang, D. Zhang, D. Wang, Z. Xu and J. Zhang, *J. Mater. Chem. A*, 2021, **9**, 14495–14506.
76 H. Yang, C. Zhu, Q. Wu, X. Li, H. Wang, J. Wan, C. Xie and D. Zeng, *Appl. Surf. Sci.*, 2022, **601**, 154213.
77 S. Rani, M. Kumar, P. Garg, R. Parmar, A. Kumar, Y. Singh, V. Baloria, U. Deshpande and V. N. Singh, *ACS Appl. Mater. Interfaces*, 2022, **14**, 15381–15390.
78 V. Galstyan, N. Kaur, D. Zappa, E. Núñez-Carmona, V. Sberveglieri and E. Comini, *Sensors*, 2020, **20**, 579.

79 A. Bertuna, G. Faglia, M. Ferroni, N. Kaur, H. M. Munasinghe Arachchige, G. Sberveglieri and E. Comini, *Sensors*, 2017, **17**, 1000.
80 P. Giannozzi, S. Baroni, N. Bonini, M. Calandra, R. Car, C. Cavazzoni, D. Ceresoli, G. L. Chiarotti, M. Cococcioni, I. Dabo, A. Dal Corso, S. de Gironcoli, S. Fabris, G. Fratesi, R. Gebauer, U. Gerstmann, C. Gougoussis, A. Kokalj, M. Lazzeri, L. Martin-Samos, N. Marzari, F. Mauri, R. Mazzarello, S. Paolini, A. Pasquarello, L. Paulatto, C. Sbraccia, S. Scandolo, G. Sclauzero, A. P. Seitsonen, A. Smogunov, P. Umari and R. M. Wentzcovitch, *J. Phys.: Condens. Matter*, 2009, **21**, 395502.
81 J. P. Perdew, K. Burke and M. Ernzerhof, *Phys. Rev. Lett.*, 1996, **77**, 3865–3868.
82 V. Barone, M. Casarin, D. Forrer, M. Pavone, M. Sambi and A. Vittadini, *J. Comput. Chem.*, 2009, **30**, 934–939.
83 D. Vanderbilt, *Phys. Rev. B: Condens. Matter Mater. Phys.*, 1990, **41**, 7892–7895.